Available online at www.sciencedirect.com
SCIENCE DIRECT®
Journal of Computational Physics 188 (2003) 434–461
JOURNAL OF COMPUTATIONAL PHYSICS
www.elsevier.com/locate/jcp

Modeling dendritic growth of a binary alloy

P. Zhao [a], M. Vénere [b], J.C. Heinrich [a,*], D.R. Poirier [c]

[a] *Department of Aerospace and Mechanical Engineering, The University of Arizona, P.O. Box 210119, 1130 N. Mountain, Tucson, AZ 85721-0119, USA*
[b] *PLADEMA-CNEA, Universidad Nacional del Centro Provincia de Buenos Aires, 7000 Tandil, Argentina*
[c] *Materials Science and Engineering, The University of Arizona, Tucson, AZ 85721, USA*

Received 29 May 2002; received in revised form 10 March 2003; accepted 11 March 2003

Abstract

A two-dimensional model for simulation of the directional solidification of dendritic alloys is presented. It solves the transient energy and solute conservation equations using finite element discretizations. The energy equation is solved in a fixed mesh of bilinear elements in which the interface is tracked; the solute conservation equation is solved in an independent, variable mesh of quadratic triangular elements in the liquid phase only. The triangular mesh is regenerated at each time step to accommodate the changes in the interface position using a Delaunay triangulation. The model is tested in a variety of situations of differing degrees of difficulty, including the directional solidification of Pb–Sb alloys.

Keywords: Dendritic solidification; Binary alloys; Finite element method; Interface tracking

1. Introduction

The importance of understanding and modeling dendritic growth remains critical to the design of manufacturing processes involving castings. The numerical modeling of alloy solidification is still a formidable task, requiring the time integration of a moving boundary problem to simulate the transport of heat and solute in the vicinity of the dendrite tips. Significant progress has been made in the simulation of single-component crystals undergoing stable or unstable solidification [1–13] when heat diffusion is the only transport mechanism, and, more recently, models that include convection have also been developed [14–16]. These models have been used to explain the effect of crystalline anisotropy on the resulting dendrite tip velocity and curvature and have been shown to agree with the results of microscopic solvability theory [17].

To predict microsegregation, however, we must be able to model constitutional inhomogeneities in multi-component alloys. This introduces a new length scale into the problem, which for steady-state solidification is $\ell_C = D_L/V$, where D_L is the mass diffusivity of the solute in the liquid phase and V is the

* Corresponding author. Tel.: +520-621-6118; fax: +520-621-8191.
E-mail address: juanh@u.arizona.edu (J.C. Heinrich).

0021-9991/03/$ - see front matter
doi:10.1016/S0021-9991(03)00185-2

solidification velocity. Because of the very low diffusivity of the solute in the melt, this diffusion length is normally several orders of magnitude smaller than the heat-diffusion length, leading to very steep concentration gradients at the solid–liquid interface, when compared to the temperature gradients, as well as to widely different time scales for the two transport processes. This makes numerical approximations to the solution of the governing equations difficult, no matter what method is used, and even though a great variety of numerical methods have been proposed for phase-change problems involving a single-component substance, few have addressed the solidification of binary alloys.

Numerical solutions to alloy solidification in one dimension were presented by Rubinsky [18] and Derby and Brown [19]. In [18], a finite element method was used to discretize the energy and solute equations; the interface was tracked with an extra moving node independent of the mesh that defined its position. The model was applied to the solidification of a dilute saline water solution, and the implications of the results on the stability of a plane front were discussed. A sophisticated numerical scheme was presented in [19] for the solution of a one-dimensional steady-state model of solidification in a vertical Bridgman furnace. A predictor–corrector in time and centered finite differences in space, in conjunction with a Newton iteration method, were used to solve the equations, and the model was applied to the solidification of the pseudo-binary alloy CdTe–HgTe.

The first attempts at finding two-dimensional solutions for binary alloys appear to be those of McCartney and Hunt [20], Ungar and Brown [21] and Tsai and Rubinsky [22]. McCartney and Hunt developed a steady-state finite difference model that solved the solute and energy equations in axisymmetric coordinates. Starting from an assumed dendrite shape and using finite differences, the mesh was chosen with mesh points lying on the interface. The energy and solute equations were solved, the computational mesh was modified to adjust the shape so it was in equilibrium with the new solution, and the procedure was iterated to convergence. The model was applied to dendritic growth on a positive temperature gradient where the influence of the growth conditions on cell tip, compositions, undercooling, tip radii, and cell spacings was examined. This model has been used in a number of publications. Subsequently, the solution of the energy equation was eliminated and temperature was included through an imposed moving linear temperature field that varied only in the axial direction [23]. Ungar and Brown analyzed the stability of a plane front solidifying directionally with a constant velocity under a prescribed temperature gradient; a ''one-sided'' model in which the solute concentration is solved only in the melt was used. The domain was fixed through a transformation that made the interface position another dependent variable to be calculated, and the equations were solved using a finite element method with bi-quadratic elements and a nonlinear Newton iteration to find cellular interfaces. This method and variations of it were also used in subsequent publications in which droplets and deep grooves were simulated [24–26]. In Ungar et al. [27], the method was extended to include the solution of the temperature field while still retaining the assumption of steady-state solidification.

Tsai and Rubinsky [22] developed a finite element model with interface tracking in which the heat flux condition at the interface was discretized using a Galerkin formulation and was used to provide additional equations to solve for the interface position. They made use of a moving mesh of quadrilateral elements that was refined at the interface, and studied the effect of transient short time temperature fluctuations on the stability of a planar interface. Somewhat later, McFadden et al. [28] developed a steady-state finite differences model for the three-dimensional calculation of non-planar interface morphologies, assuming a linear temperature field and using their iterative method as a false time. It was applied to the solidification of Al–Cr alloys, in which steady-state solutions revealed two-dimensional bands and three-dimensional hexagonal nodes.

Palle and Dantzig [29] developed an adaptive mesh finite element method for the solidification of binary alloys based on a fixed grid of bilinear elements that is locally refined in the proximity of the interface. They used linear triangles to handle the mesh transitions, and the refinement was controlled by the local error using an error estimator. The energy equation was formulated in terms of enthalpy, with the position of the interface recovered from the freezing isotherm. The solute conservation equation was formulated in terms

of the chemical activities, making them of the same form as the energy equation. The method was applied to two-dimensional solidification in a square region where the temperature at the lower left corner was reduced below the solidus temperature and the boundaries were assumed to be adiabatic. Results were presented for the solidification of Fe—0.05 wt% C. A full thermosolutal model using a fixed mesh was developed by Juric [30]. This was a direct extension of the model for a single substance presented in [9]. Juric used a single-field representation for the liquid and solid phases in which the jump in material properties at the interface is implicitly included and he assumed equal liquid and solid densities. These methods use a material indicator function similar to the phase-field variable, but the material indicator function is determined from the position of the tracked interface and only used to express the physical properties and the single-field variable. The equations are solved on a fixed mesh. The model was applied to directional solidification in a rectangular region starting from a perturbed plane front, and the analysis of Mullins and Sekerka [31] was used to determine the domain dimension and to ensure that the system was unstable. The results showed a necking phenomenon in growing granular protrusions and the actual pinch-off of solid granules. Simulations on a grid of 200 by 600 points, intended to show the formation of dendrites during directional solidification, revealed resolution difficulties due to the explicit nature of the algorithm. These simulations were then performed assuming a known linear temperature field in the growth direction.

Models based on boundary integrals and the solution of an integro-differential equation were proposed in [32,33], respectively. Both used one-sided models to solve for the solute field only and calculated steady-state solutions. Other work involving numerical simulations of dendritic solidification of binary alloys has been done using the phase-field method [34–42]. In all of these works, the temperature field was prescribed and only the solute concentrations were calculated. Warren and Boettinger [38] applied the phase-field equations to a Ni–Cu alloy in a constant temperature field. The equations were solved by means of a finite difference method using a uniform grid, and some simplifying assumptions had to be made to make the problem tractable. They obtained very realistic growth patterns that captured the development, coarsening and coalescence of secondary and tertiary dendrite arms, however.

For the directional solidification problems of interest here, solidification is effected under a stable temperature gradient, but, as we show, the assumption of a constant temperature gradient is not valid in our case because the latent heat is significant in the metallic alloys under consideration, the interface deviates significantly from planar, and the alloys are not dilute. Therefore, the temperature and solute concentration fields have to be calculated simultaneously. In this paper, we present a model based on the direct solution of the coupled energy and solute conservation equations using finite element discretizations. The energy equation is written in terms of temperature only, and is solved using the front-tracking method of [13], which uses a fixed finite element mesh for the temperature and describes the moving interface by means of a set of marker points that are defined at every time and that move according to the interface conditions. The solute conservation equation is solved in a separate adaptive mesh of triangular elements that is very fine at and next to the interface so that the solute diffusion length scale ℓ_C can be resolved. This mesh is regenerated at every time step to accommodate the interface motion, and the information from the last mesh is passed on to the new one by interpolation. The energy and solute equations are coupled at the interface.

In the following section, we present the mathematical model; the finite element method and mesh generation procedures are discussed in Section 3; in Section 4 we show the results of computations; and Section 5 closes with a discussion of the results and conclusions.

2. Mathematical model of solidification

We assume that the physical properties are different but constant in each phase, the latent heat is independent of the solute concentration and therefore constant, and the densities of the solid and liquid

phases are equal so fluid flow by shrinkage or natural convection is ignored. The diffusion-limited process of solidification (melting) of a binary alloy is then governed by the energy and solute conservation equations given by

$$\frac{\partial T_S}{\partial t} = Le_S \nabla^2 T_S \quad \text{in the solid} \tag{1a}$$

and

$$\frac{\partial T_L}{\partial t} = Le_L \nabla^2 T_L \quad \text{in the liquid.} \tag{1b}$$

At the solid–liquid interface we have the conditions

$$T_S = T_L = T_I \tag{2a}$$

and

$$(\eta Le_S \nabla T_S - Le_L \nabla T_L) \cdot \mathbf{n} = \left[\frac{1}{St} + \beta(T_I - T_m)\right] V. \tag{2b}$$

In the equations above, the subscripts S and L denote the solid and liquid phases, respectively; $\mathbf{n}$ is the unit vector normal to the interface pointing into the liquid; and V is the local normal interface velocity. The equations have been non-dimensionalized using a reference length H, the solute diffusion timescale H^2/D_L, and the characteristic velocity D_L/H. With the dimensional temperature as T^*, the non-dimensional temperature is chosen as $T = (T^* - T_E)/\Delta T$, where $\Delta T = T_{m0} - T_E$; T_{m0} is the melting point of the pure solvent; and T_E is the eutectic temperature. The non-dimensional parameters are the ratio of the volumetric heat capacities in the solid and liquid $\eta = \rho c_{PS}/\rho c_{PL}$, the Lewis numbers $Le_S = \alpha_S/D_L$ and $Le_L = \alpha_L/D_L$, the Stefan number $St = c_{PL}\Delta T/L$, and the difference in non-dimensional specific heat $\beta = (c_{PL} - c_{PS})/c_{PL}$. Here, D_L is the solute diffusion coefficient, L is the latent heat, and $\alpha_S = \kappa_S/\rho c_{PS}$ and $\alpha_L = \kappa_L/\rho c_{PL}$ are the thermal diffusivities, with κ_S and κ_L the thermal conductivities. The non-dimensional temperatures T_I and T_m denote the local interface and equilibrium liquidus temperatures, respectively.

We are interested primarily in metallic alloys, and the solute diffusion in the solid is several orders of magnitude smaller than in the liquid. Hence, the solute diffusion in the solid is neglected, and the solute concentration is solved only in the liquid. The solute concentration is made non-dimensional using the initial concentration C_0, that is, $C_L = C_L^*/C_0$, where the asterisk denotes a dimensional variable. In the liquid it is given by

$$\frac{\partial C_L}{\partial t} = \nabla^2 C_L, \tag{3}$$

with the interface conditions,

$$(-\nabla C_L) \cdot \mathbf{n} = (1-k) C_L V \quad \text{before the eutectic solidification} \tag{4a}$$

and

$$C_L = C_E \quad \text{at the eutectic solidification.} \tag{4b}$$

Eq. (4a) applies at the interface except when solidification of the eutectic composition occurs; then, Eq. (4b) applies.

The temperature at a coordinate on the interface depends on the curvature at the coordinate. For a two-dimensional interface in x–y coordinates, we define $\mathbb{C}^*$ as twice the dimensional curvature [43],

$$\frac{\mathbb{C}^*}{2} = \frac{y''}{[1+y_I'^2]^{3/2}}, \tag{5a}$$

where y' and y'' are the first and second derivatives, respectively, of the interface given as $y(x)$. Twice the non-dimensional curvature is

$$\mathbb{C} = H\mathbb{C}^*. \tag{5b}$$

Details pertaining to the numerical determination of the curvature of the interface can be found in [13]. The local interface temperature is given by the generalized Gibbs–Thompson relation

$$T_I - T_m + (1 + mC_L)\sigma\mathbb{C} + \mu V + \beta St(T_I - T_m)^2 = 0. \tag{6}$$

In Eqs. (4a) and (6), $\sigma = T_{m0}\gamma/\rho LH\Delta T$ and $\mu = D_L/Hv\Delta T$ are non-dimensional surface tension and kinetic mobility, respectively; k is the equilibrium partition ratio, assumed constant; γ is the dimensional surface energy; v is the kinetic mobility; and the liquidus of the phase diagram is approximated by the linear relation $T_m = 1 + mC_L$, where m is the non-dimensional slope of the liquidus line. The derivation of Eq. (6) is given in Appendix A.

3. Numerical method

Eqs. (1a), (1b) and (3) are reformulated using Galerkin weighted residuals and solved using the finite element method. The treatment of the energy equation remains the same as in [13], and so it is not repeated here. One of the most challenging difficulties in obtaining the solution of the coupled system of equations (1a)–(6) stems from the disparity between the heat diffusion length, $\ell_T = \alpha_L/V$, and the solute diffusion length, $\ell_C = D_L/V$, in the liquid; these differ by roughly four orders of magnitude in the metallic alloys considered in this work. In order to resolve the much thinner solute concentration boundary layer ahead of the solidification front, a method based on the solution of the energy and solute conservation equations in independent meshes has been chosen. The temperature is calculated over a fixed mesh of rectangular bi-linear elements in which the interface can move freely according to the interface dynamics determined by Eqs. (2a) and (2b). The interface is defined by a set of marker points that move with it, as shown in Fig. 1. Marker points can be added if they drift too far apart or removed if they get too close together to maintain the resolution of the interface (details of this part of the algorithm are explained in [13]). On the other hand, the solute concentration equation is discretized over an independent adaptive grid of linear or quadratic triangular elements. This grid is extremely fine close to the interface in order to adequately resolve the length scale ℓ_C at the interface, and the elements increase in size very quickly away from the interface. Details of this procedure are explained next.

3.1. Discretization of the solute concentration equation

Because coupling between the solute concentration and the temperature equations occurs only at the solid–liquid interface through the local melting temperature T_m in Eq. (6), there is no need to evaluate the solute concentration field at the nodes where the temperature is calculated. The strategy adopted to calculate the solute concentration is as follows:

1. At time $t = t_n$, the temperature, concentration, interface position, and velocity of each marker in the direction normal to the interface are known.
2. A new interface position is obtained by moving each marker on the interface in the normal direction according to its known velocity. The spacing between markers is checked, and markers are added and/or deleted if necessary.

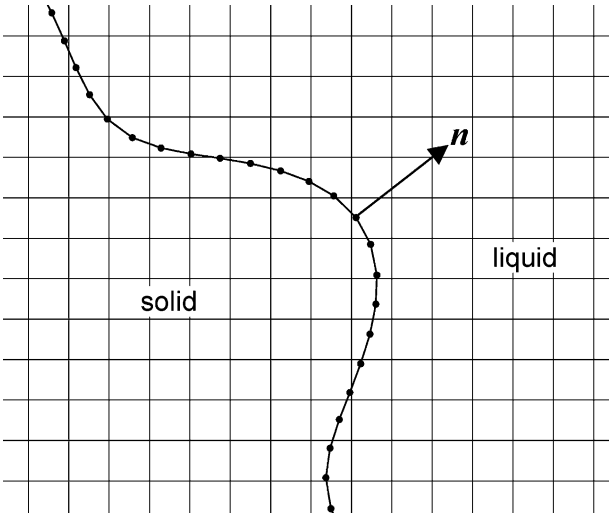

Fig. 1. Schematic of a solidification interface described by marker points over a fixed uniform finite element mesh and advancing in its normal direction.

3. A mesh of triangular elements conforming to the new interface position is generated.
4. The solute concentration at the last time step is interpolated from the old mesh to the new mesh.
5. Using the current interface velocity, a new temperature is calculated from Eqs. (1a) and (1b), and a new solute concentration is calculated from Eq. (3).
6. The local melting temperature at the interface is calculated from $T_m = 1 + mC_L$, and the interface temperature is then calculated from Eq. (6).
7. A new interface velocity is calculated for each marker from Eqs. (2a) and (2b) and is compared with the previously available velocity. If the relative difference at each marker is less than the prescribed tolerance, the time step is complete and a new time step is started from step 1. Otherwise, a new interface velocity is obtained at each marker, and the program goes back to step 5.

The solution of Eqs. (3), (4a), and (4b) is done by means of a standard weighted residuals form; that is, these equations are re-written in the form

$$\int_{\Omega_L} \left(W \frac{\partial C_L}{\partial t} + \nabla W \cdot \nabla C_L \right) d\Omega = \int_{\Gamma} W(1-k) C_L V \, d\Gamma, \tag{7}$$

where W is a weighting function, Ω_L is the portion of the domain Ω that contains the liquid, and Γ is the interface. The solute concentration is expressed in terms of shape functions as

$$C_L(\mathbf{x}, t) = \sum_i N_i(\mathbf{x})(C_L)_i(t). \tag{8}$$

The weighting functions are set equal to the shape functions in a Galerkin formulation, and the time derivative is discretized using the θ-method [44, p. 260]. The element equations become

$$(\mathbf{M} + \theta \Delta t \mathbf{K})\mathbf{C}_L^{n+1} = (\mathbf{M} + (\theta - 1)\Delta t \mathbf{K})\mathbf{C}_L^n + \mathbf{F}^n, \tag{9}$$

where $\mathbf{C}_L^n$ denotes the vector of nodal values at time $t = t_n$. The matrices are

$$\mathbf{M} = \int_e N_i N_j \, d\Omega, \tag{10a}$$

$$\mathbf{K} = \int_e \nabla N_i \cdot \nabla N_j \, \mathrm{d}\Omega, \tag{10b}$$

and the vector $\mathbf{F}^n$ has components

$$F_i^n = \int_{\Gamma_e} N_i (1-k) \left(\sum_j N_j (C_L)_j^n \right) \bar{V}_e \, \mathrm{d}\Gamma. \tag{10c}$$

Here, e denotes the element under consideration, Γ_e is the portion of the interface coinciding with a side of the element, if any, and $\bar{V}_e$ is the average interface velocity in the element. The linear system of equations, Eq. (9), is solved using a conjugate gradient iterative method [45]. In this work, the value $\theta = 0.5$ has been used, which yields an accuracy that is second order in time.

3.2. Mesh generation

The solute concentration equation is solved in the liquid only. The solutal diffusion length, ℓ_C, is very small compared with the thermal diffusion length, and the interface shape changes at every time step and can become extremely contorted. Thus, an adequate strategy is needed for dealing with these constraints in an accurate and efficient manner. A number of adaptive strategies have been proposed to accommodate the change from one time step to the next [46]. The ones most commonly used are based on moving the nodes while conserving the mesh structure [47]. Another strategy consists of selecting elements according to an error criterion and subdividing them in such a way as to preserve the mesh quality [48,49]. Because the interfaces can become very complex and the computational domain over which the solute conservation equation is solved changes continuously, these methods have been deemed impractical for the present problem. Instead, the decision was made to perform a complete re-meshing of the liquid region at each time step, in order to avoid problems associated with excessive deformation of the elements and the resulting degradation of the mesh quality. The price paid for this is that a full interpolation of the solutal field from the old to the new mesh is required at each time step. This may introduce excessive interpolation error that violates mass conservation; more details follow.

The process used in the generation of the meshes involves three stages: (1) The sizes of the elements are specified by means of a size function $S(x, y)$, which in most cases is an error function. In this work the elements are refined according to their normal distance to the solid–liquid interface. (2) A mesh is generated from the size function and the mesh of the previous time step using the method described in [50]. (3) The solute concentration is interpolated from the old mesh to the new one. Because each of these procedures must be performed at every time step and the meshes required in the computations typically contain $O(10^4$–$10^5)$ elements, efficiency becomes a key issue in the mesh generation. The present implementation achieves a $O(N \log N)$ computational cost, where N is the number of elements in the mesh. This allows the whole process to be performed at a cost similar to that of the calculation of the temperature field and the position of the interface.

The size function is obtained using the previous mesh as a background mesh and interpolating with the same shape functions used in the finite element discretization. To obtain a computational cost of $O(N \log N)$, the elements of the background mesh are classified using a quadtree [51] in such a way that every "terminal square" contains, at most, one mesh node, as explained in [52]. The whole domain is first enclosed in a square region that becomes the root of the quadtree. Then the mesh nodes are inserted in such a way that, every time two nodes lie in the same square, this square is subdivided into four squares, until, in the final quadtree, no square contains more than one mesh node and many contain none. This procedure is illustrated in Fig. 2. When this process is finished, each terminal square is intersected by only a small number of mesh elements. A list is then generated that contains all the elements with some portion of their

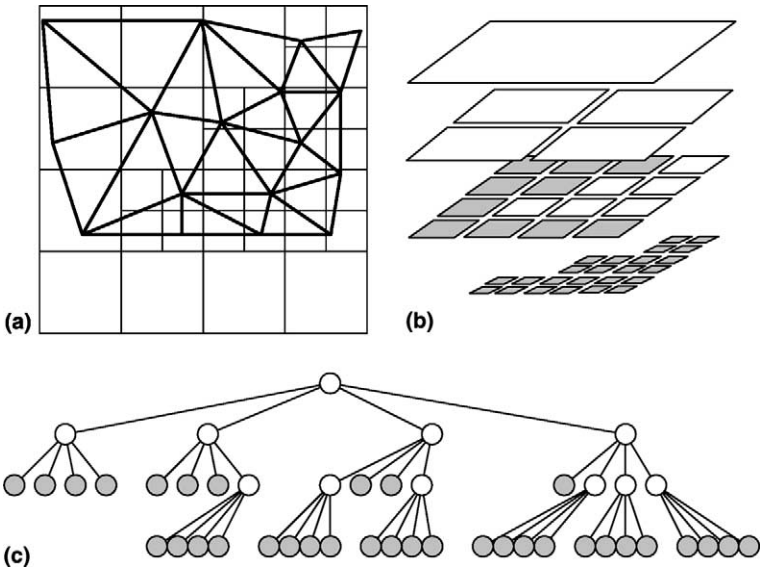

Fig. 2. Mesh structure development using the quadtree: (a) mesh and resulting quadtree partitioning using the criterion "one node or less per terminal square"; (b) the four levels of partitioning in the resulting quadtree; (c) representation of the data structure.

area in each terminal square. It is among these elements that we now search for the element that contains the new node that is inside the terminal. For each node of the new mesh, a search of the terminal that contains the node is done with a cost $O(\log N)$. The search for the element in the old mesh that contains the node is done on the elements associated with the terminal at a fixed cost, and, finally, the interpolation inside the element also has a fixed cost so the whole process for all the nodes remains $O(N \log N)$.

The generation of the mesh of triangular elements is accomplished with a special implementation of the Delaunay method [51], in which nodes are added incrementally. The method involves three steps: starting with a two triangle subdivision of the root square of the quadtree described above, the nodes that define the domain boundary are added; next, the domain boundary is recovered and the external elements contained in the root square that do not belong to the domain are removed; and, finally, the interior elements are generated. This procedure is illustrated in Fig. 3. In Fig. 3(a), we observe a large number of spurious connections in the region occupied by the interface, because every marker point has been defined as a boundary point. During the mesh generation, the nodes are added sequentially, maintaining the Delaunay condition that the interior of the circumcircle of each triangle must not contain any node of the triangulation. The triangulation obtained is the convex hull of the set of nodes, as can be seen in Fig. 3(a). During this part of the process, it is possible to miss some boundary edges. Therefore, before removing the external elements, the boundary must be checked and, if necessary, recovered. Finally, new nodes are added to elements selected for refinement in the interior of the domain by dividing the largest element side into two, as shown in Fig. 3(c). New elements are generated, joining the new node to the opposite vertices. Once the new elements have been generated, the quadrilateral regions defined with adjacent elements are analyzed to see whether changing the orientation of the diagonal yields better-shaped elements. If this is the case, then the change is made, and the new elements are analyzed again with respect to their new neighbors. If the quality criteria used to decide when to make the change is the maximization of the minimum angle, the triangulation generated will be of the Delaunay type. Furthermore, if the order in which the elements are subdivided is properly chosen, then the number of elements that need to be analyzed is bounded and does not depend on the overall size of the mesh [53].

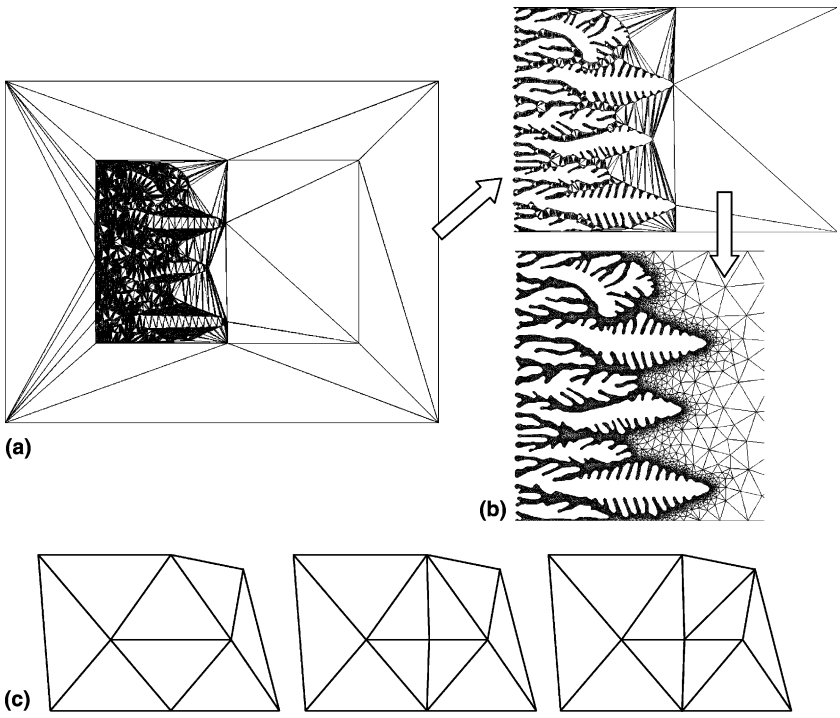

Fig. 3. Mesh generation process: (a) generation of the boundary nodes; (b) elimination of external elements and generation of interior nodes; (c) addition of interior nodes to the Delaunay mesh.

An adaptive grid method for dendritic solidification of a pure substance using the phase-field method has been successfully used by Provatas et al. [11]. Their method differs significantly from this one in that it is not based on a Delaunay triangulation but, instead, uses a quadtree-generated mesh with bilinear quadrilateral elements combined with linear triangular transition elements to accommodate the extra nodes produced on the side of an element when a rectangle is subdivided. The present method utilizes only triangular elements in the solution of the solute concentration equation. Furthermore, as mentioned above, it has been determined that in order to conserve mass accurately in the solute conservation equation it is necessary to use quadratic triangular elements [44]. Because of the exponentially decaying nature of the solute boundary layer ahead of the dendrite tips, linear interpolation from the mesh used in the last time step to the new mesh for the next time step always overestimates the interpolated variable, due to the lack of curvature of the linear triangular element. In time, the interpolation error produces an increase of the solute mass, unless extremely small linear elements are used within a distance of approximately $5\ell_C$ of the advancing interface. This makes the meshes based on linear triangular elements overly large and impractical. On the other hand, it has been determined through numerical experiments that using quadratic triangular elements, which are capable of approximating the curvature in the exponentially decaying solute field, results in the possibility of using meshes containing about one tenth the number of linear elements and one half the number of nodes, relegating the error in the mass conservation to less than 0.1% at the end of a typical calculation.

3.3. Accuracy

The present algorithm considers the solution of the thermal field and interface position independently from that of the solute concentration field. In [13], we showed through numerical experiments that the

algorithm used to obtain the temperature and interface position approximates these with second-order accuracy in space. On the other hand, quadratic elements must approximate the solution to the solute concentration equation with third-order accuracy [44]. It is therefore reasonable to expect that the algorithm is probably $O(h^2, \Delta t^2)$ when the Crank–Nicolson–Galerkin method is used in the time discretization, where h is the mesh size in the solution of the energy equation. However, it would be very difficult to produce a meaningful example to illustrate this.

A similarity solution can be obtained in one dimension for a particular case where the melt is initially at a uniform temperature, and then the temperature at the left end, $x = 0$, is lowered below the freezing temperature at time $t > 0$, [54]. Eqs. (1a), (1b), and (3) are solved in the semi-infinite interval $0 \leqslant x < \infty$ with initial conditions $T(x, 0) = T_0$, $C_L(x, 0) = C_0$, and $x_I(0) = 0$, where T_0 and C_0 are constants, T_0 is equal to or higher than the freezing temperature of $T_m(C_0)$, and x_I denotes the position of the interface as a function of time. The boundary conditions are $T_S(0, t) = T_1$, $T_L(\infty, t) = T_0$, and $C_L(\infty, t) = C_0$, where T_1 is lower than $T_m(C_0)$. In dimensional form, the solution is

$$x_I(t) = 2\lambda\sqrt{\alpha_S t}, \tag{11}$$

$$T_S = T_1 + (T_I - T_1)\frac{\operatorname{erf}(x/2\sqrt{\alpha_S t})}{\operatorname{erf}(\lambda)}, \tag{12}$$

$$T_L = T_0 + (T_I - T_0)\frac{\operatorname{erfc}(x/2\sqrt{\alpha_L t})}{\operatorname{erfc}\left(\lambda\sqrt{\alpha_S/\alpha_L}\right)}, \tag{13}$$

$$C_L = C_0 + (C_I - C_0)\frac{\operatorname{erfc}\left(x/2\sqrt{D_L t}\right)}{\operatorname{erfc}\left(\lambda\sqrt{\alpha_S/D_L}\right)}, \tag{14}$$

where λ, T_I, and C_I are obtained from

$$\frac{k_S(T_I - T_1)e^{-\lambda^2}}{\sqrt{\alpha_S}\operatorname{erf}(\lambda)} + \frac{k_L(T_I - T_0)e^{-\lambda^2\alpha_S/\alpha_L}}{\sqrt{\alpha_L}\operatorname{erfc}\left(\lambda\sqrt{\alpha_S/\alpha_L}\right)} = \rho L\lambda\sqrt{\pi}, \tag{15}$$

$$C_I = \frac{C_0}{1 - (1-k)\sqrt{\pi\alpha_S/\alpha_L}\lambda e^{\lambda^2\alpha_S/\alpha_L}\operatorname{erfc}\left(\lambda\sqrt{\alpha_S/D_L}\right)}, \tag{16}$$

$$T_I = T_{m0} + mC_I. \tag{17}$$

In one-dimensional solidification under a temperature gradient G in the liquid, analytic expressions for the steady-state solute profile in the liquid and solidification velocity can be obtained, assuming that the interface velocity becomes constant. From Eq. (2b), ignoring the kinetic mobility and assuming that the thermal diffusivity is large, the steady-state velocity is given by

$$V_A = \frac{-\kappa_L G + \sqrt{(\kappa_L G)^2 + 4\rho L\kappa_S R}}{2\rho L}. \tag{18}$$

In this equation, R is the cooling rate applied as the boundary condition at the left end of the interval ($x = 0$). In a coordinate system moving with the interface, the steady-state concentration in the liquid is given by

$$C_L(x) = C_0\left[1 + \left(\frac{1-k}{k}\right)\exp\left(-\frac{V_A}{D_L}x\right)\right]. \tag{19}$$

These expressions are used to assess the accuracy of the algorithm in one dimension.

4. Solidification simulations

In order to validate the numerical model developed in this work, the model is first applied to one-dimensional solidification. The alloy of interest is Pb–Sb. The physical properties used in this work are given in Table 1. First, a calculation is presented for comparison with the analytical solution presented in Section 3. The initial temperature is $T_0 = T_m(C_0)$ and $T_1 = T_0 - 10$ (K). Under these conditions, the parameter λ from Eq. (15) is $\lambda = 0.004149053$, and the interface solute concentration and temperature are $C_I = 3.65811857$ wt% and $T_I = T_0 - 9.95749171$ (K). The solute concentration over a finite domain 2 mm long, with a uniform fixed mesh of 200 linear elements to solve for the temperature and 200 quadratic elements in a variable mesh for the solute concentration, is shown in Figs. 4 and 5. Fig. 4(a) shows the calculated interface position as a function of time, together with the relative error, which is less than 0.01% throughout the calculation. Fig. 4(b) is a similar plot of the interface velocity as a function of time; the error is slightly larger, as expected, but is still very small. The calculated and analytical solutions are indistinguishable when plotted together. Fig. 5(a) shows the solute concentration at four different times, and Fig. 5(b) shows the relative error in the concentration. The errors are of the same order as for the interface position. At the beginning of the calculation, the error is larger because, in the analytical solution, the interface concentration goes instantaneously from C_0 to C_I while the numerical method needed a few time steps to reach it.

Several one-dimensional calculations have been performed under a variety of different conditions; here, we present one such calculation that illustrates the results. The domain is 20 mm long, initially a temperature gradient of 10 K/mm is imposed with $T_m(C_0)$ at $x = 0$, and the initial solute concentration is uniform and equal to 2.2 wt% Sb. At time $t > 0$, a cooling rate of 0.1 K/s is applied at the left end of the

Table 1
Physical properties of a Pb–Sb alloy

Property	Symbol and unit	Value
Bulk concentration of Sb	C_0, wt%	2.2
Solute diffusivity	D_L, mm^2/s	1.13×10^{-3}
Solute partition ratio	k	0.312
Eutectic concentration	C_E, wt%	11.2
Slope of liquidus line	m, K/wt%	−6.829
Melting temperature of pure solvent	T_{m0}, K	600.0
Eutectic temperature	T_E, K	523.5
Density	ρ, kg/mm^3	1.0416×10^{-5}
Specific heat of solid	c_{PS}, J/kg K	142.0
Specific heat of liquid	c_{PL}, J/kg K	151.0
Heat conductivity in the solid	κ_S, J/s mm K	0.030
Heat conductivity in the liquid	κ_L, J/s mm K	0.016
Thermal diffusivity in the solid	α_S, mm^2/s	20.28
Thermal diffusivity in the liquid	α_L, mm^2/s	10.17
Lewis number in the solid	Le_S	17947
Lewis number in the liquid	Le_L	9000
Latent heat of fusion	L, J/kg	29775
Surface energy	γ, J/mm^2	7.0×10^{-8}
Kinetic mobility	v, mm/s K	6.67

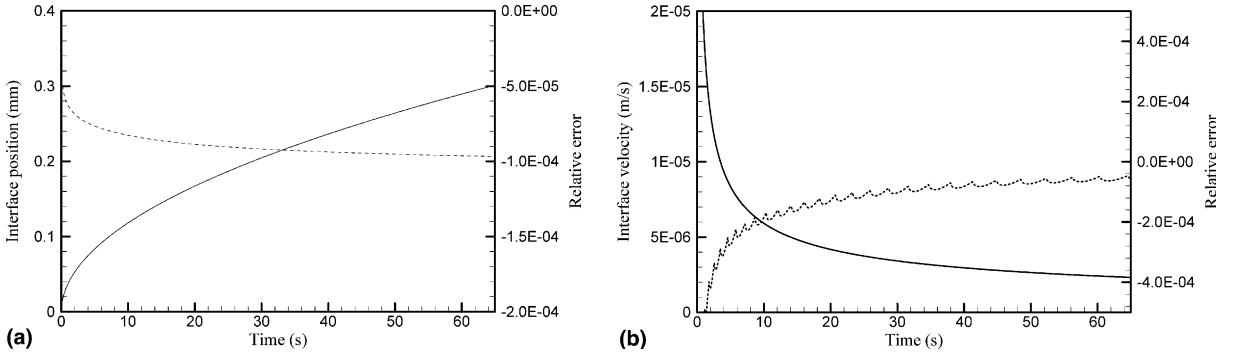

Fig. 4. Comparison of calculated finite element results and the analytical solution given by Eq. (14): (a) calculated interface position and relative error (broken curve); (b) calculated interface velocity and relative error (broken curve).

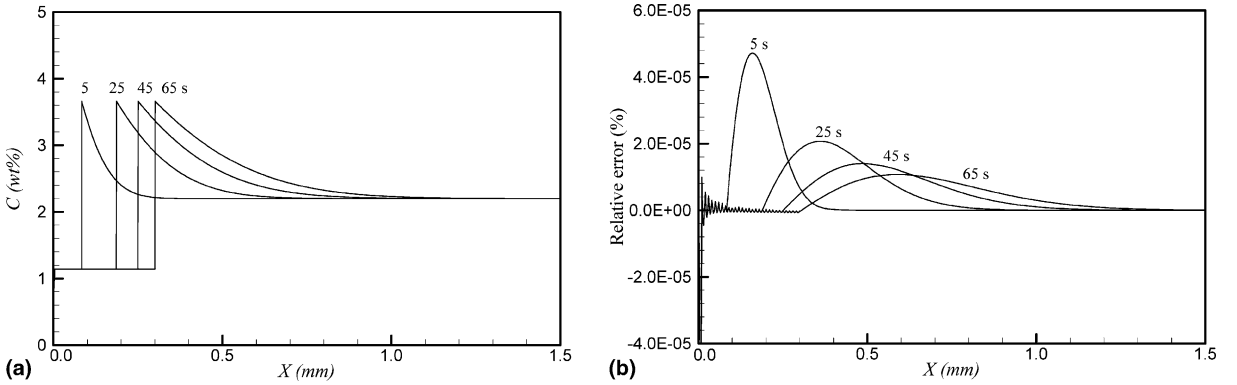

Fig. 5. Comparison of the calculated finite element results and the analytical solution of Eq. (14) at times 5, 25, 45, and 65 s: (a) calculated solute concentration; (b) relative error in the solute concentration.

domain ($x = 0$), and the initial temperature gradient is imposed on the right boundary. This domain is long enough for the solidification velocity to approximate steady-state and to be compared with V_A, given by Eq. (18). For the present problem, $V_A = 1.801 \times 10^{-2}$ mm/s.

Figs. 6(a) and (b) show results obtained, with the temperature discretized by fixed linear one-dimensional elements and the solute concentration discretized with a changing mesh of quadratic one-dimensional elements, at time 900 s when the interface is at approximately 10 mm. Fig 6(a) shows the temperature, which has been shifted down by $T_m(C_0)$. The difference between the calculated temperature and the temperature $T_m(C_L)$ corresponding to the liquidus of the local solute concentration is shown with a dashed line. A region of constitutional undercooling can be observed just in front of the interface, which extends for about 3 mm ahead of the interface (about fifty times the diffusion length). The temperature field shows a clear deviation from a constant temperature gradient at the interface. The observed change in the temperature gradient at the interface is due to the large difference in thermal conductivity between the solid and the liquid; this has a larger effect than does the latent heat release and causes the concave shape in the temperature profile. The solute boundary layer shows a maximum of 7.073 wt%, which differs by 0.3% from the steady-state value, C_0/k. The interface velocity calculated in this case is 1.807×10^{-2} mm/s, a deviation of 0.3% from V_A of Eq. (18). The concentration in the solid has been obtained from $C_S = kC_L$ at the interface since the eutectic concentration is not reached, and the total solute mass conservation shows no error. The solute concen-

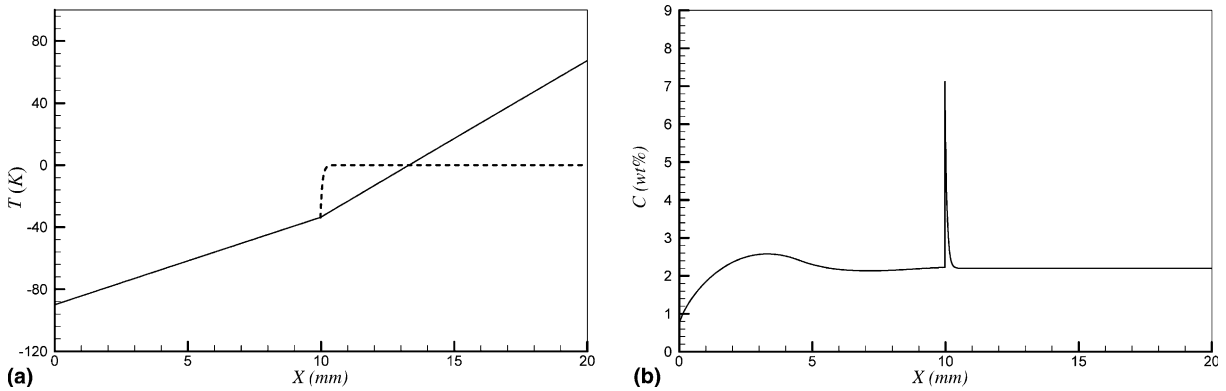

Fig. 6. One-dimensional solidification of a Pb-2.2 wt% Sb alloy. (a) Temperature distribution: the solid line is the calculated temperature; the dashed line is the liquidus temperature calculated from the phase diagram according to the local solution concentration. (b) Solute concentration.

tration calculated in the solute boundary layer is shown in Fig. 7, together with the one calculated from Eq. (19). They are undistinguishable. The maximum difference in this case is only 0.3% with respect to the analytic concentration.

A two-dimensional example that considers growth of an equiaxial grain in an undercooled solution without an imposed thermal gradient is now discussed in order to illustrate the effect of a second component and to compare its behavior with that of a pure substance. The case of a pure substance is presented in Fig. 7 of [9], Fig. 21 of [12], and Fig. 12 of [13]. In non-dimensional form, the domain is a square, four units on a side, and a seed is placed in the center. The boundaries of the square are assumed to be adiabatic, and at the start of the calculation, the solid and liquid are at uniform temperatures: $T_S = 0$ and $T_L = -0.5$. The shape of the seed is given by $x = x_c + R\cos(\theta)$ and $y = y_c + R\sin(\theta)$, where (x_c, y_c) is the center of the region and $R = 0.1 + 0.02\cos(4\theta)$. The non-dimensional surface tension and the non-dimensional kinetic mobility are both 0.002. The thermal diffusivity and heat capacity in the solid and liquid are the same.

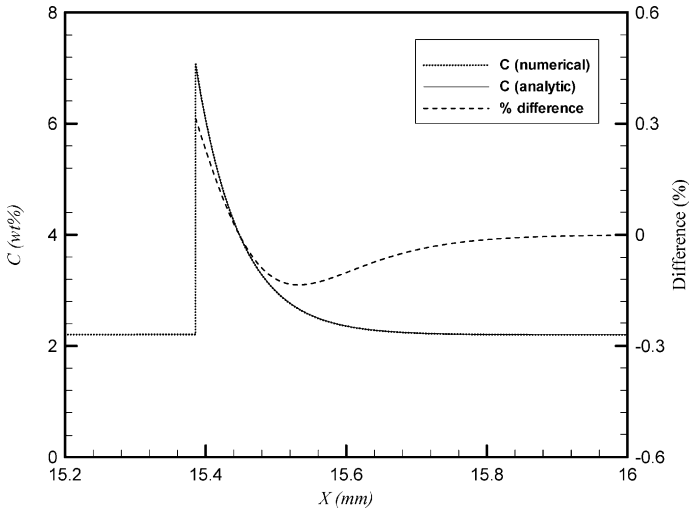

Fig. 7. Comparison of the calculated solute concentration field in Fig. 6(b) with the steady-state analytical solution in the vicinity of the interface position.

The results of two calculations in non-dimensional form are presented: the first assumes a pure substance and does not include the solute; the second considers an alloy with $C_0 = 2.2$, $Le_L = 10.0$, and $m = -0.035$. In the latter case, the values of the Lewis number Le_L and the slope of the liquidus line m are much smaller than those of the Pb–Sb alloys of interest, but large enough to clearly illustrate the effect of the presence of the alloy on the solidification process. Initially the concentration of solute in the seed is assumed to be kC_0, the concentration in the solid deposited at the interface is obtained from $C_S = kC_l$. The small size of the domain utilized in previous calculations (four by four) leads to an interaction between the adiabatic thermal boundaries and the interface morphology. Therefore to maintain the far-field values of the temperature at the boundary, the energy equation in these calculations is solved in a larger domain of twenty units on a side. Imbedded in this domain is the smaller 4 by 4 subdomain in which the interface tracking and the solution of the solutal concentration equation take place. The mesh to solve the energy equation consists of a uniform mesh of 200 by 200 square elements in the subdomain and a non-uniform mesh of linear triangular elements outside the subdomain. The non-uniform mesh becomes coarse away from the subdomain, where the temperature gradients are small. Fig. 8(a) illustrates such a mesh with a smaller number of elements than used in the actual calculations for better clarity. The full domain, the interface position, and the temperature field at $t = 1.0$ for the case of a pure substance are shown in Fig. 8(b), where it is clearly seen that the domain boundary does not interfere with the thermal boundary layer.

Fig. 8(c) shows that the pure substance solidifies much faster than the alloy, and that the morphologies of the dendrites are different. The alloy shows much thinner and longer grooves, and the tips show a tendency to begin to split. The solutal concentration field in both the solid and liquid is shown in Fig. 8(d), the solutal boundary layer ahead of the interface as well as a slight amount of microsegregation in the solid can be observed. Figs. 8(e) and (f) show the temperature fields, with the interface demarcated as a broken line, at time $t = 1.0$ for the pure substance and the alloy, respectively. We observe that the solid region in the alloy is below $T_m(C_0)$ while in the pure substance it is always slightly above.

Results of a calculation using $Le_L = 100.0$ and $m = -0.1$ at $t = 2.0$ are presented in Fig. 9. The larger value of Le_L produces a thinner solutal boundary layer in the liquid, and the more pronounced slope of liquidus line in the phase diagram slows down the interface growth further. This case is used to illustrate the adaptive meshes generated during the calculation of solutal concentration field. Fig. 9(a) shows the interface at $t = 2.0$, very narrow grooves and more splitting of the tips are observed. Fig. 9(b) shows the solutal concentration in the solid and the liquid, the solutal boundary layer is significantly narrower than in the previous case. Fig. 9(c) shows the mesh of triangular elements at time $t = 2.0$ in the first quadrant of the domain, and a detail of the same mesh that zooms into the thin long groove at 45 degrees is depicted in Fig. 9(d). The high quality of the meshes obtained with the procedure described in Section 3.2 can be clearly observed in both Figs. 9(c) and (d).

The next set of results uses the data of the calculations performed by Ungar and Brown [24]. The exact conditions described in this reference cannot be achieved here, because they assumed that the temperature gradient was prescribed and constant and they neglected the latent heat. The latter assumption cannot be imposed in this model; nevertheless the results can be compared to those of [24]. The thermophysical properties listed in their earlier work [21] are used.

The computational domain is 2 mm by 0.6 mm. The width of the domain was chosen to obtain six cells, each with the width of the preferred wavelength ($\lambda^* = 0.1$ mm) of the unstable interface. In order to obtain initial conditions as close as possible to those used in [24], the calculations were first performed in one dimension as explained below. Initially, in one dimension, a linear temperature gradient G^* is imposed with temperature $T_m(C_0)$ at $x = 0$. For time $t > 0$, a cooling rate is applied at $x = 0$, and the initial temperature gradient is imposed on the right boundary. The one-dimensional domain is long enough for solidification to reach a steady state. The cooling rate Cr is adjusted so that the steady-state velocity gives Peclet numbers, $Pe = V\lambda^*/D_L$, equal to those used in [24]. The non-dimensional temperature gradient G is given in terms of the dimensional quantities $(*)$ by the expression $G = G^*\lambda^*/T^*_{m0}$.

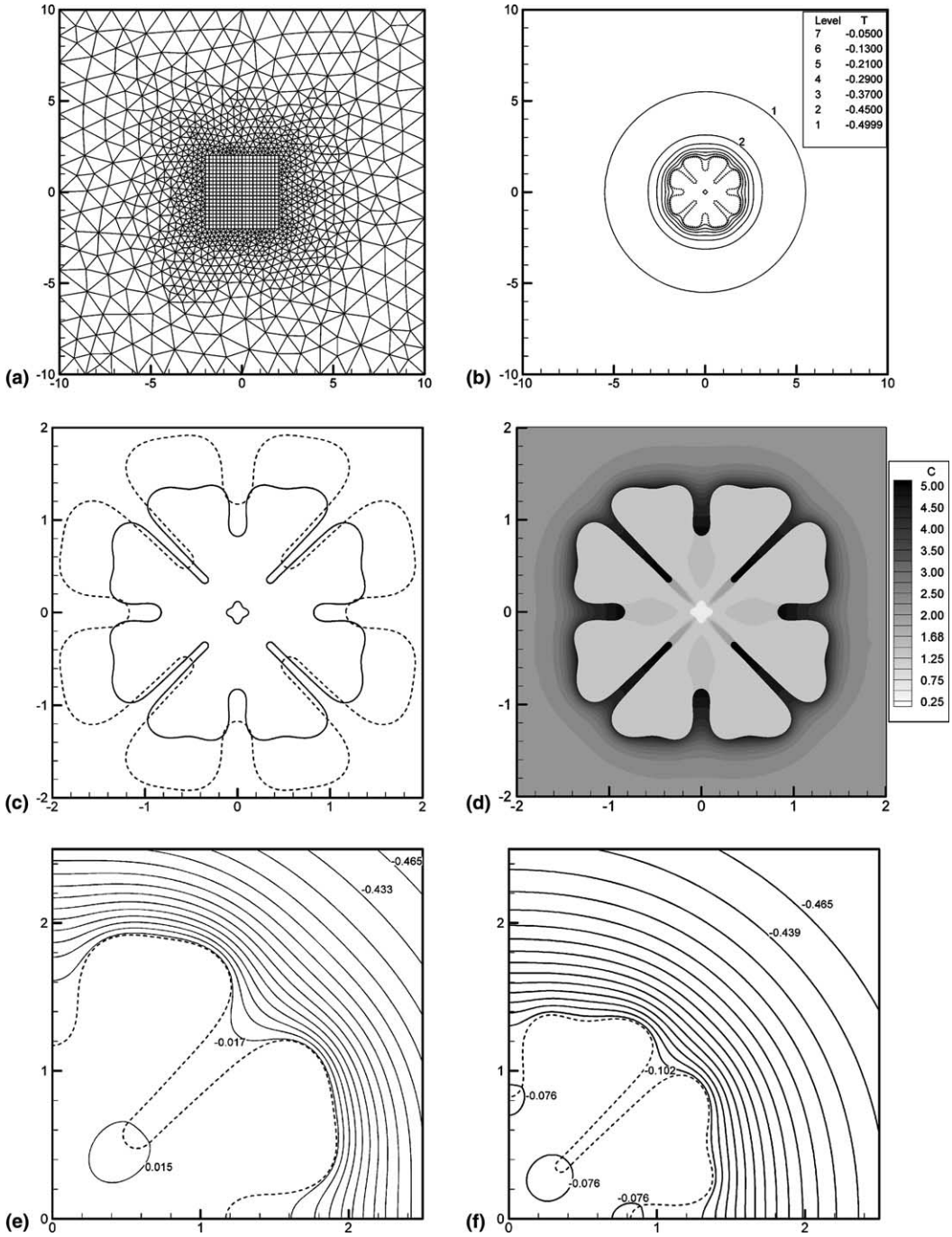

Fig. 8. Growth of an equiaxial grain into an undercooled liquid. (a) Mixed computational domain: energy equation is solved everywhere; solutal concentration equation is solved only in the liquid phase within the square subdomain in the center. (b) Temperature field and interface position for the case of a pure substance in the full domain at $t = 1.0$. (c) Comparison of the morphology between the pure substance (dashed line) and the alloy (solid line) at $t = 1.0$. (d) Solutal concentration in the alloy at $t = 1.0$. (e) Temperature field for the pure substance at $t = 1.0$. (f) Temperature field for the alloy at $t = 1.0$.

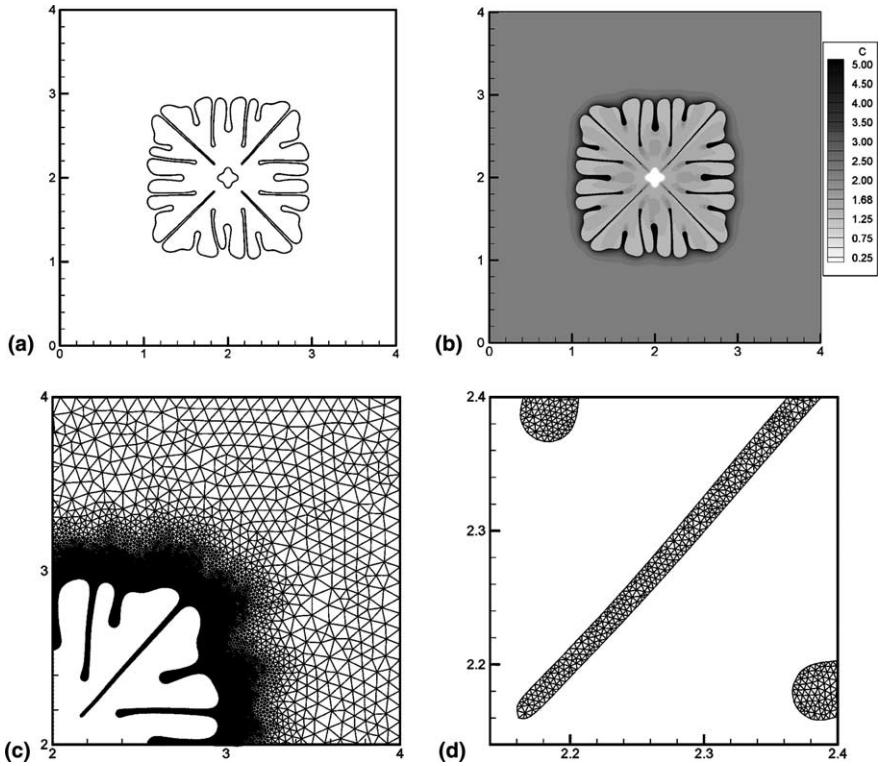

Fig. 9. Equiaxial growth of alloy with $Le_L = 10.0$ and $m = -0.1$ at $t = 2.0$: (a) dendritic morphology; (b) solute concentration; (c) triangular-element mesh in the first quadrant; (d) detail of (c) in the grooves.

The steady-state temperature and solute concentration fields obtained from the one-dimensional calculation are used as initial conditions for the two-dimensional calculation, starting from a planar interface with the same cooling rate applied at $x = 0$ and with the temperature gradient G^* imposed on the right-hand side ($x = 2$ mm). The two-dimensional model is subsequently run for 100 time steps to verify that the steady-state velocity does not change and, at this point, the perturbation is introduced. The front is perturbed with the same wavelength as in [24] and a perturbation amplitude of $0.01\lambda^*$. The perturbation is introduced at only one time step, and the cellular morphology is allowed to develop. All of these calculations have been performed using a mesh of 100 by 30 bilinear elements for the temperature field. The solute concentration equation is solved in a variable mesh of quadratic triangular elements with a minimum size less than 20% of the solutal diffusion length at the interface. The initial mesh contains close to 12,000 elements. Table 2 summarizes the calculations, including the CPU time in a 400 MHz Silicon Graphics Origin 2000 computer at The University of Arizona using a single processor.

In [24], $Pe = 0.8$ was used. At this Péclet number, in the presence of latent heat, the linear stability analysis of Mullins and Sekerka [31] predicts that the interface is stable, which has been confirmed in our numerical calculations. Figs. 10(a) and (b) show the linear stability curves predicted by the Mullins and Sekerka model for a non-dimensional thermal gradient of 1.68×10^{-4} and several values of the Péclet number, neglecting and including the latent heat, respectively. It can be clearly seen that the interface is marginally unstable for $Pe = 0.8$ in the absence of latent heat (Fig. 10(a)), but is stable in the presence of the latent heat given in Table 1 (Fig. 10(b)). It can also be observed how the most unstable wavelength, given by the maximum in the curves, shifts towards the left as the Péclet number increases, resulting in narrower cells.

Results for $Pe = 1.0$ are shown in Figs. 11(a) and (b) up to 60 s of solidification. Fig. 11(a) shows the position of the interface at intervals of 3 s. In this and the rest of the results presented here, the interface is shown starting from the time the planar interface is perturbed. This case is very close to the stable limit, and the perturbation takes some time to develop into a pattern of shallow waves. Fig. 11(b) shows the solute concentration at the end of the calculation, where some weak microsegregation in the solid is evident after the instability has developed. The shape of the cellular front predicted with the present model differs from that shown in Fig. 5a of [24] for the same temperature gradient, in that no grooves develop here and the tips of the cells are round and not flattened.

Figs. 12(a) and (b) show results for $Pe = 1.4$ for 40 s of solidification. For a higher Péclet number, the instability develops sooner, the tips of the cells are flattened, and we observe more microsegregation in the solid. The cells have grooves and resemble more the ones in [24], but no deep grooves can be detected. This

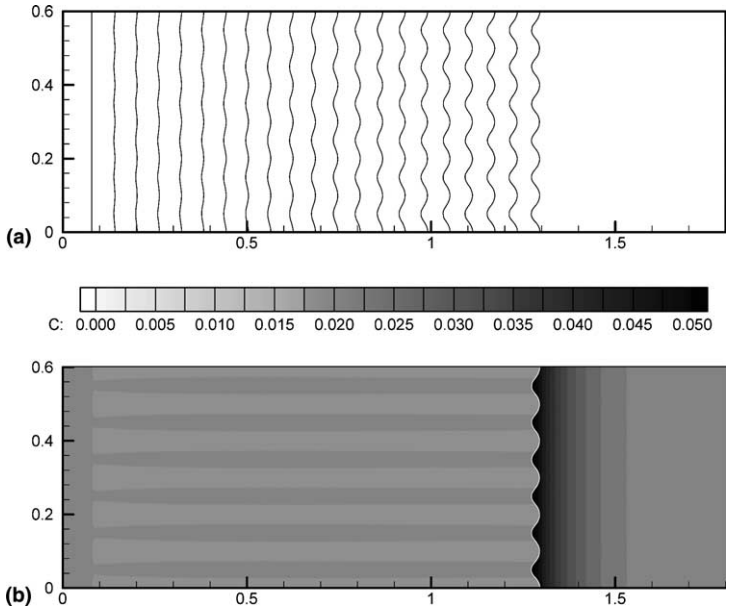

Fig. 11. Solidification from a perturbed plane front with a non-dimensional thermal gradient of 1.68×10^{-4} and Péclet number 1.0: (a) interface position at intervals of 3 s; (b) solute concentration at 60 s (the interface is white).

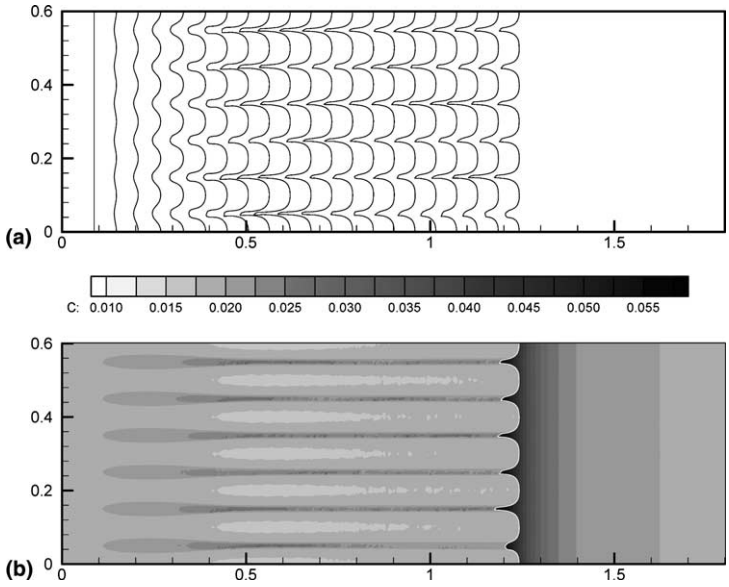

Fig. 12. Solidification from a perturbed plane front with Péclet number 1.4 and a non-dimensional thermal gradient 1.68×10^{-4}: (a) interface position at intervals of 2 s; (b) solute concentration at 40 s (the interface is white).

The third case is for $Pe = 2.15$, and the results are shown in Figs. 13(a) and (b) for 26 s. From Fig. 13(b) we see that the original perturbation with $\lambda^* = 0.1$ mm does not have the correct preferred wavelength; the cells split shortly after the instability develops but not all the new cells survive. Four of them die somewhat

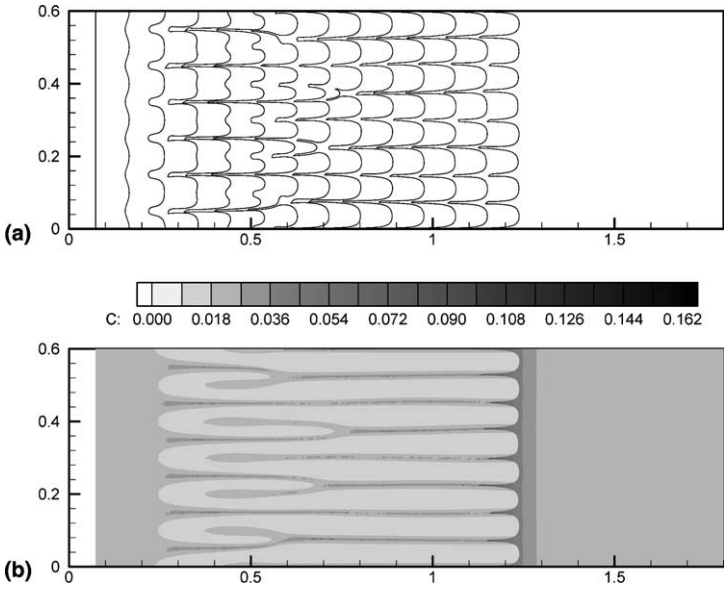

Fig. 13. Solidification from a perturbed plane front with Péclet number 2.15 and a non-dimensional temperature gradient 1.68×10^{-4}: (a) interface position at intervals of 2 s; (b) solute concentration at 26 s (the interface is white).

later, and the system goes from six initial cells to eight, where it stabilizes at a wavelength of about $0.75\lambda^*$ in accordance with Fig. 10(b). For $Pe = 1.4$, two calculations with different temperature gradients are shown in Figs. 14(a) and (b) for 38 s and in Figs. 15(a) and (b) for 46 s. In the first of these, $G = 0.5 \times 10^{-4}$, the ratio G/Pe is smaller than before, indicating a more unstable situation. In Figs. 14(a) and (b), we observe

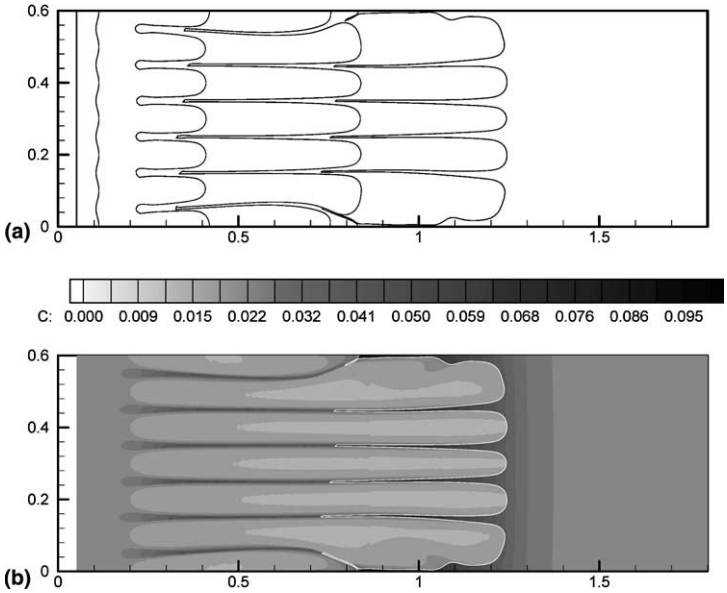

Fig. 14. Solidification from a perturbed plane front with Péclet number 1.4 and a non-dimensional temperature gradient 0.5×10^{-4}: (a) interface position at 0, 2, 10, 24, and 38 s; (b) solute concentration at 38 s (the interface is white).

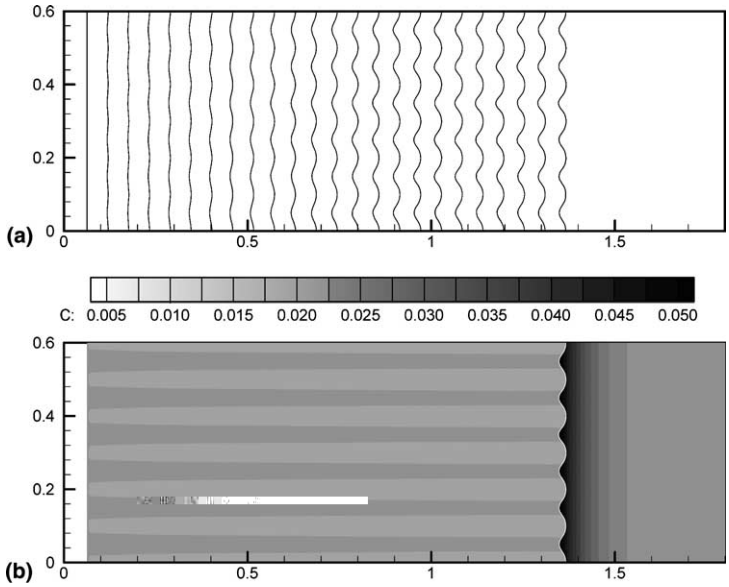

Fig. 15. Solidification from a perturbed plane front with Péclet number 1.4 and a non-dimensional temperature gradient 2.33×10^{-4}: (a) interface position at intervals of 2 s; (b) solute concentration at 46 s (the interface is white).

deep cells, the depth of the cells increase with time and, at the end of the calculation, only five of the original six cells survive. Figs. 15(a) and (b) show results for $G = 2.33 \times 10^{-4}$. This case has practically the same value of the ratio G/Pe as case 1 in Table 2, and the results are indeed very similar in both cases.

To further investigate the ability of the cells to evolve to the preferred wavelength, the case with $Pe = 1.4$ and $G = 1.68 \times 10^{-4}$ was repeated, one time starting from a single perturbation in the center of the domain and another time with a random perturbation. Figs. 16(a) and (b) show the calculation with a single perturbation midway up the vertical interface; initially a single cell develops, but later the system settles to the same six cells as in case 2 in Table 2. A similar situation is observed in Figs. 17(a) and (b) where a random perturbation is applied along the plane interface. Initially many protuberances develop, but they quickly consolidate into six cells.

The next calculation presented here is for a Pb–Sb alloy with a concentration of 2.2 wt% Sb. This concentration is two orders of magnitude larger than that used in [24]. The properties for Pb-2.2 wt% Sb are given in Table 1. These are somewhat different from those in [21] due to the significant difference in the initial solute concentration. For these alloys, the buildup of solute concentration at the interface is large and so is the effect of the solute concentration on the temperature of the interface. The stronger nonlinear coupling between the solute concentration and temperature makes the numerical simulations difficult, and the system is very unstable and convergence is slower. Mullins and Sekerka's [31] analysis predicts that the most unstable wavelengths at the onset of instability are much smaller at large solute concentrations. To overcome the strong numerical instability, a very small time step must be used. Furthermore, solidification is extremely slow at the beginning of the process because the buildup of solute at the interface greatly lowers the freezing temperature. Numerical experiments have shown that, for the cooling rates of interest, the solidification is very slow at first and, for a long period of time, the interface barely advances while the concentration increases enough to cause constitutional undercooling and trigger the instability. In order to save computational time, the one-dimensional model is run first. The temperature, concentration profiles, and interface position from the one-dimensional calculation are then used as initial conditions to start the full two-dimensional calculations.

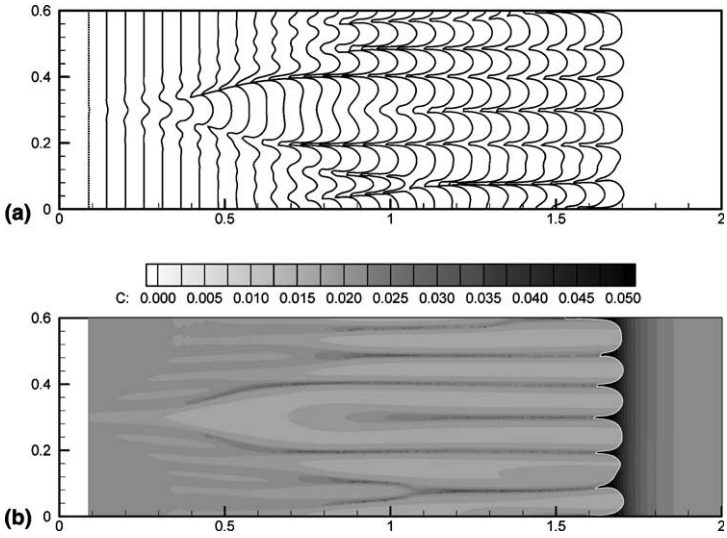

Fig. 16. Solidification from a perturbed plane front with Péclet number 1.4 and a non-dimensional temperature gradient 1.68×10^{-4} perturbing the plane front at the single location $y = 0.3$: (a) interface position at intervals of 2 s; (b) solute concentration at 56 s (the interface is white).

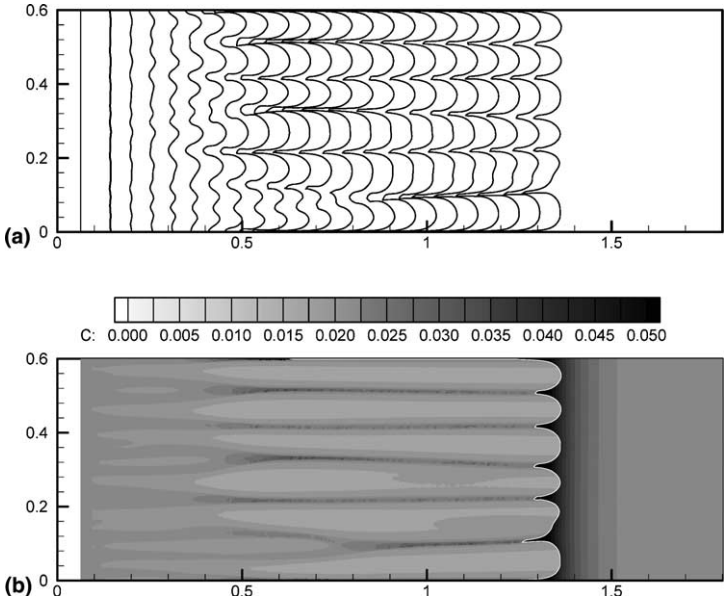

Fig. 17. Solidification from a perturbed plane front with Péclet number 1.4 and a non-dimensional temperature gradient 1.68×10^{-4}, starting with a random perturbation: (a) interface position at intervals of 2 s; (b) solute concentration at 44 s (the interface is white).

For Pb-2.2 wt% Sb, the applied temperature gradient is 10 K/mm, and the applied cooling rate is 0.1 K/s. The one-dimensional simulation is stopped when $C_I = 4.69$ wt% Sb and $V = 3.79$ μm/s. Based on the above concentration and velocity, the theory of Mullins and Sekerka [31] predicts a most unstable wavelength of about 10 μm. To resolve this small length scale, a domain of 0.8 by 0.24 mm was chosen; the mesh for the

temperature calculation consisted of 30 by 100 bilinear elements, and the mesh for the solute concentration initially contained 80 quadratic elements along the planar interface. During the simulation, the total number of elements in a mesh ranges between 10,000 and 25,000, and the number of nodes ranges between 40,000 and 100,000. The non-dimensional surface tension is anisotropic, given by $\sigma_n(\theta) = \sigma[1 + 0.4(8/3\sin^4(2\theta) - 1)]$, and the kinetic mobility is constant.

Fig. 18 shows the results after 26 s of simulation from the time the perturbation, with a wavelength of 40 μm is applied. Fig. 18(a) shows that the first protuberances to grow are very small, actually slightly smaller than expected, with an average wavelength of 7 μm. However, the system very quickly evolves to larger structures, and at the end of the calculation, the computational region seems to be able to hold only one branched primary dendrite arm. This "cascading" of length scales as the dendritic structures evolve appears to be one of the main difficulties in the successful numerical simulation of dendritic solidification of alloys. For the alloy and conditions under consideration, experimental measurements show a primary dendrite spacing on the order of 150–200 μm [55], which is more than an order of magnitude larger than

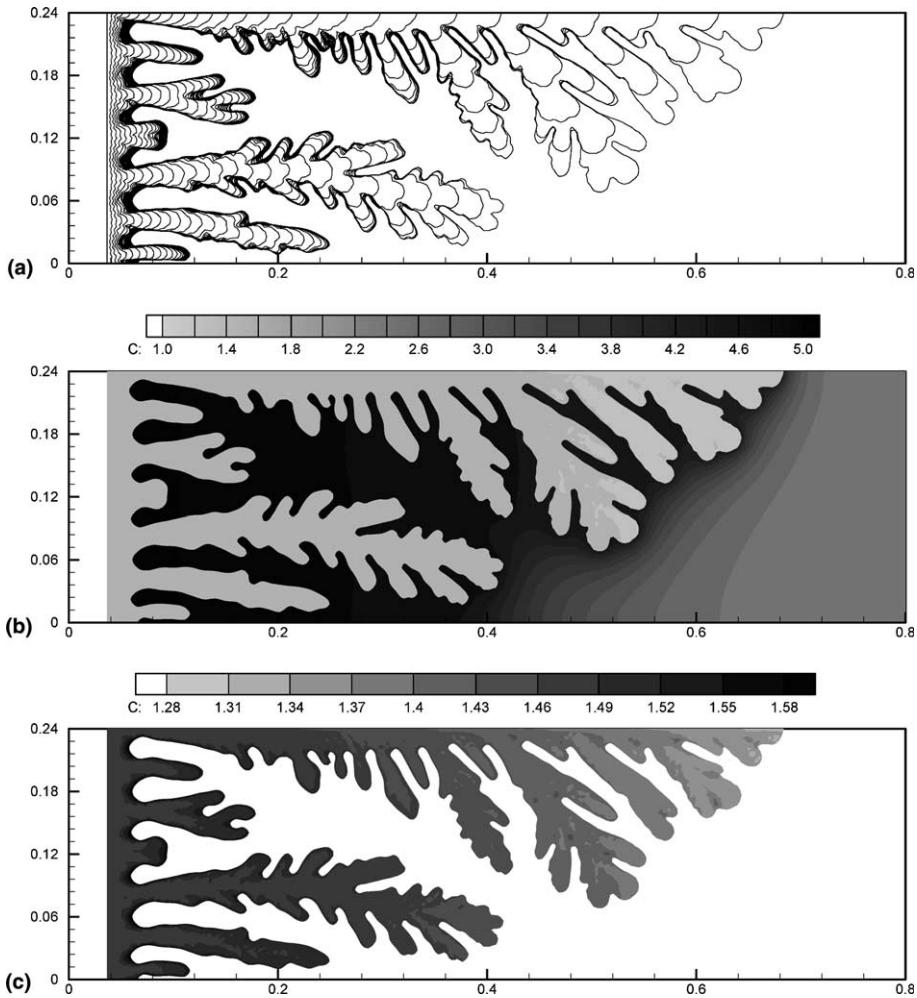

Fig. 18. Solidification of a Pb-2.2 wt% Sb alloy after 26 s: (a) interface position at intervals of 1 s; (b) Solute concentration at 26 s; (c) solute concentration in the solid at 26 s.

that of the original linear instability. However, if one wishes to study the evolution of a dendritic structure from a planar interface, then the small-scale instability must be resolved to provide the correct initial conditions, which makes the computational effort quite formidable. Fig. 18(b) shows the solute concentration at 26 s. The largest concentration at the base of the dendrites has reached about 5 wt% Sb. Fig. 18(c) shows the concentration in the solid only, which varies over a smaller range, but clearly shows the concentration in the solid increasing at the base of the dendrites due to the accumulation of solute in the interdendritic liquid. Fig. 19 shows the temperature field at 26 s. The temperature is not constant along a fixed value of x, nor linear in the x-direction along fixed values of y. The deviations from a fixed constant gradient, although expected, are surprisingly large.

For the alloy with 5.8 wt% Sb, the calculation was performed in a region 2 mm long by 0.8 mm high using a mesh of 40 by 100 bilinear elements for the temperature field and a mesh with 120 quadratic triangles on the initial planar interface. The temperature gradient is 10 K/mm and the cooling rate 0.4 K/s. The two-dimensional calculation was started from a one-dimensional plane front when the interface solute concentration was 7.46 wt% Sb and the interface velocity was 1.53 μm/s. A larger perturbation with wavelength 0.1 mm was used purposely to inhibit the small initial protuberances at the interface; these large perturbations quickly grow and evolve into dendritic cells. Results after 96 s of simulation are shown in Fig. 20. In Fig. 20(a) the interface position is shown at intervals of 2 s, and it can be seen that, in the first interface profile at 2 s, the very small protuberances have already disappeared. Fig. 20(b) shows the solute concentration at 96 s. The position of the interface is white. The solid region reaches more than 1.2 mm in the x-direction everywhere in the domain. Because a eutectic composition is reached at the roots of the dendrites, the microstructure in the solid exhibits significant microsegregation. The primary dendritic structure has an average concentration of less than 3.5 wt% Sb, and the interdendritic solid is comprised of the eutectic mixture, with a concentration very close to the eutectic concentration of 11.2 wt% Sb. In this simulation, we have not calculated the morphological features of the eutectic mixture. The non-dimensional solute concentration in the eutetic solid at the eutectic solidification is given by

$$C_{\mathrm{SE}} = C_{\mathrm{E}} + \frac{1}{Le_{\mathrm{L}} V}\mathbf{n}\cdot\nabla C_{\mathrm{L}}. \tag{20}$$

Hence, the concentration of the eutectic solid can be anywhere between kC_{E} and C_{E}, depending on the interface velocity and the solute concentration gradient in the liquid side of the interface. Eutectic solidification occurs at the roots of the dendrites where the solute concentration gradient is small and the solidification velocity is large. According to Eq. (20), the concentration in the eutectic solid is approximately equal to C_{E}; hence, the concentration in the solid undergoes a sudden change, roughly from kC_{E} in the primary solid to C_{E} in the eutectic solid.

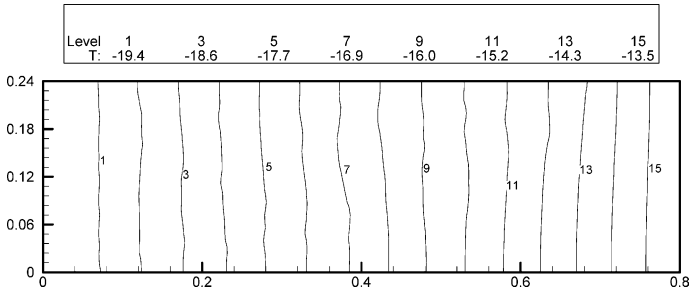

Fig. 19. Temperatures in solidification of Pb-2.2 wt% Sb alloy at time 26 s.

5. Conclusion

At this point, some calculations are difficult to perform and require a very large amount of computer time because very small time steps and a large number of nonlinear iterations within each time step are required to achieve convergence. There are three physical parameters that complicate the calculations: the small solute diffusivity relative to the heat diffusivity that creates a disparity in the length and time scales; the large solute concentration that significantly reduces the preferred wavelength of the instability when starting from a plane front; and the large values of the slope of the liquidus m, in that small changes in the interface concentration are greatly magnified (by a factor >6.8 in the case of a Pb–Sb alloy). The latter appears to be a source of instability when the interface temperature is calculated through the Gibbs–Thompson equation. The model is capable of computing effectively when any two of these parameters are realistic; however, when all three are set to practical levels, the calculations become slow and difficult. Ways to resolve this difficulty are still under investigation.

The presence of a solute produces very small morphological features that lead to a variety of problems with the mesh generation. As a result, it cannot be claimed that all the numerical difficulties related to the advance of the interface deep in the mushy zone have been resolved. Fortunately this has little effect on the general dendritic structure, and no effect on the dendrite tips.

Several alternative algorithms have been considered in this work, including that which appears to be the most attractive option of calculating over two fixed meshes of bilinear elements with different resolution. None of the alternatives appears to be as versatile and accurate as the one presented here. The present model has shown that it can be applied to simulations of real materials—these calculations are the first of their kind. All the physical features that we expect are captured, and comparisons with available results using other models show good agreement.

Acknowledgements

This work was supported by the National Aeronautics and Space Administration under Grant NCC8-96 and by the National Science Foundation under Grant DMR 0072955.

Appendix A. Derivation of Eq. (6)

The effect of curvature of an interface on the undercooling of the interface can be found in Alexiades and Solomon [54]. In dimensional form, the undercooling can be found from

$$(c_{\mathrm{PL}} - c_{\mathrm{PS}})\left[T_{\mathrm{I}} \ln\left(\frac{T_{\mathrm{I}}}{T_{\mathrm{m}}}\right) - T_{\mathrm{I}} + T_{\mathrm{m}}\right] + L\left(\frac{T_{\mathrm{I}}}{T_{\mathrm{m}}} - 1\right) + \frac{\gamma \mathbb{C}}{\rho_{\mathrm{S}}} = 0. \tag{A.1}$$

Eq. (A.1) applies to a pure substance with a fixed melting point of T_{m}. The surface tension of the interface is γ, and the interface temperature is T_{I}. It is also assumed that both phases are incompressible, and have constant densities and specific heats, and that the pressure change in the liquid (or the concomitant pressure change in the solid) can be ignored. We include a term for the kinetic mobility of the interface and rewrite Eq. (A.1) as

$$T_{\mathrm{I}} - T_{\mathrm{m}} + \frac{T_{\mathrm{m}}(c_{\mathrm{PL}} - c_{\mathrm{SL}})}{L}\left[T_{\mathrm{I}} \ln\left(\frac{T_{\mathrm{I}}}{T_{\mathrm{m}}}\right) + T_{\mathrm{m}} - T_{\mathrm{I}}\right] + \frac{T_{\mathrm{m}}\gamma}{L\rho_{\mathrm{S}}}\mathbb{C} + \frac{V}{v} = 0, \tag{A.2}$$

where V is the normal component of the velocity of the interface and v is the kinetic mobility (m s^{-1} K^{-1}).

The undercooling of a metallic interface between the solid and liquid is small. Hence, we invoke the approximation

$$\ln\left(\frac{T_I}{T_m}\right) \cong -\frac{T_I - T_m}{T_m}.$$

Eq. (A.2) becomes

$$T_I - T_m + \frac{c_{PL} - c_{PS}}{L}(T_I - T_m)^2 + \frac{T_m\gamma}{L\rho_S}\mathbb{C} + \frac{V}{v} = 0. \tag{A.3}$$

In order to apply Eq. (A.3) to the solid–liquid interface of a binary alloy, the melting point is interpreted as the liquidus of the alloy; thus

$$T_m = T_{m0} + mC_L, \tag{A.4}$$

where the liquidus on the phase diagram is assumed to be linear with a slope m, C_L is the concentration of the alloy element in the liquid at the interface, and T_{m0} is the melting point of the major component of the alloy (i.e., the solvent).

In Eqs. (A.3) and (A.4), we substitute the following non-dimensional variables:

$$\sigma = \frac{T_{m0}\gamma}{\rho_S L\Delta TH} \quad \text{(non-dimensional surface tension)},$$

$$\mu = \frac{D_L}{v\Delta TH} \quad \text{(non-dimensional kinetic mobility)},$$

$$\tilde{V} = \frac{HV}{D_L}, \quad \tilde{\mathbb{C}} = H\mathbb{C},$$

$$\tilde{m} = m\frac{C_0}{\Delta T}, \quad \tilde{C} = \frac{C_L}{C_0}.$$

With these substitutions and dropping the tilde over the non-dimensional variables, Eq. (6) is obtained.

References

[1] C. Bonacina, G. Comini, A. Fasano, M. Primicerio, Numerical solution of phase change problems, Int. J. Heat Mass Transfer 21 (1973) 1825.
[2] L.A. Crivelli, S.R. Idelsohn, A temperature-based finite element solution for phase-change problems, Int. J. Numer. Methods Engrg. 23 (1986) 99.
[3] J.M. Sullivan, D.R. Lynch, K. O'Neil, Finite element simulations of planer instabilities during solidification of an undercooled melt, J. Comput. Phys. 69 (1987) 81.
[4] V.R. Voller, S.M. Swaminathan, B.G. Thomas, Fixed grid techniques for phase change problems, Int. J. Numer. Methods Engrg. 30 (1990) 875.
[5] K. Trivestoris, R.A. Brown, Boundary-conforming mapping applied to computation of highly deformed solidification surfaces, Int. J. Numer. Methods Fluids 14 (1992) 981.
[6] J.A. Sethian, J. Strain, Crystal growth and dendritic solidification, J. Comput. Phys. 98 (1992) 231.
[7] R. Almgren, Variational algorithms and pattern formation in dendritic solidification, J. Comput. Phys. 106 (1993) 337.
[8] A.A. Wheeler, B.T. Murray, R.J. Schafer, Computation of dendrites using a phase field model, Physica D 66 (1993) 243.
[9] D. Juric, G. Tryggvason, A front-tracking method for dendritic solidification, J. Comput. Phys. 123 (1996) 127.
[10] A. Karma, W.J. Rappel, Quantitative phase-field modeling of dendritic growth in two and three dimensions, Phys. Rev. E 57 (1998) 4323.
[11] N. Provatas, N. Goldenfeld, J. Dantzig, Adaptive mesh refinement computation of solidification microstructures using dynamic data structures, J. Comput. Phys. 148 (1999) 265.

[12] H.S. Udaykumar, R. Mittal, W. Shyy, Computation of solid–liquid phase fronts in the sharp interface limit on fixed grids, J. Comput. Phys. 153 (1999) 535.
[13] P. Zhao, J.C. Heinrich, Front-tracking finite element method for dendritic solidification, J. Comput. Phys. 173 (2001) 765.
[14] R. Tönhardt, G. Amberg, Phase-field simulation of dendritic growth in a shear flow, J. Cryst. Growth 194 (1998) 406.
[15] C. Beckermannn, H.-J. Diepers, I. Steinbach, A. Karma, X. Tong, Modeling melt convection in phase-field simulations of solidification, J. Comput. Phys. 154 (1999) 468.
[16] J.-H. Jeong, N. Goldenfeld, J.A. Dantzig, Phase-field model for three-dimensional dendritic growth with fluid flow, Phys. Rev. E 64 (2001) 041602.
[17] D.I. Meiron, Selection of steady-states in the two-dimensional symmetric model of dendritic growth, Phys. Rev. A 33 (1986) 2704.
[18] B. Rubinsky, Solidification processes in saline solutions, J. Cryst. Growth 62 (1983) 513.
[19] J.J. Derby, R.A. Brown, A fully implicit method for simulation of the one-dimensional solidification of a binary alloy, Chem. Engrg. Sci. 41 (1986) 37.
[20] D.G. McCartney, J.D. Hunt, A numerical finite difference model of steady-state cellular and dendritic growth, Metall. Trans. A 15A (1984) 983.
[21] L.H. Ungar, R.A. Brown, Cellular interface morphologies in directional solidification; the one-sided model, Phys. Rev. B 29B (1984) 1367.
[22] H.L. Tsai, B. Rubinsky, A numerical study using "front tracking" finite elements on the morphological stability of a planar interface during transient solidification processes, J. Cryst. Growth 69 (1984) 29.
[23] S-Z. Lu, J.D. Hunt, A numerical analysis of dendritic and cellular array growth: the spacing adjustment mechanisms, J. Cryst. Growth 123 (1992) 17.
[24] L.H. Ungar, R.A. Brown, Cellular interface morphologies in directional solidification; IV. The formation of deep cells, Phys. Rev. B 31B (1985) 5931.
[25] N. Ramprasad, M.J. Bennett, R.A. Brown, Wavelength dependence of cells of finite depth in directional solidification, Phys. Rev. B 38B (1988) 583.
[26] M.J. Bennett, R.A. Brown, Cellular dynamics during directional solidification: interaction of multiple cells, Phys. Rev. B 39B (1989) 705.
[27] L.H. Ungar, M.J. Bennett, R.A. Brown, Cellular interface morphologies in directional solidification; III. The effect of heat transfer and solid diffusivity, Phys. Rev. B 31 (1985) 5923.
[28] G.B. McFadden, R.F. Boisvert, S.R. Coriell, Nonplanar interface morphologies during directional solidification of a binary alloy, J. Cryst. Growth 84 (1987) 371.
[29] N. Palle, J.A. Dantzig, An adaptive mesh refinement scheme for solidification problems, Metall. Mater. Trans. A 27A (1996) 707.
[30] D. Juric, Computations of phase change, Ph.D. Dissertation, University of Michigan, Ann Arbor, 1996.
[31] W.W. Mullins, R.F. Sekerka, Stability of a planar interface during solidification of a dilute alloy, J. Appl. Phys. 35 (1964) 444.
[32] Y. Saito, G. Goldbeck-Wood, H. Müller-Krumbhaar, Numerical solution of dendritic growth, Phys. Rev. A 38A (1988) 2148.
[33] D.A. Kessler, H. Levin, Steady-state cellular growth during directional solidification, Phys. Rev. A 39A (1989) 3041.
[34] A.A. Wheeler, W.J. Boettinger, G.B. McFadden, Phase-field model for isothermal phase transitions in binary alloys, Phys. Rev. A 45 (1992) 7424.
[35] H. Löwen, J. Berchoefer, L.S. Tuckerman, Crystal growth at long times: critical behavior at the crossover from diffusion to kinetic-limited regimes, Phys. Rev. A 45 (1992) 2399.
[36] G. Caginalp, W. Xie, Phase-field and sharp-interface alloy models, Phys. Rev. E 48 (1993) 1897.
[37] A. Karma, Phase-field model of eutectic growth, Phys. Rev. E 49 (1994) 2245.
[38] J.A. Warren, W.J. Boettinger, Prediction of dendritic growth and microsegregation patterns in a binary alloy using the phase-field method, Acta Metall. Mater. 43 (1995) 689.
[39] A.A. Wheeler, G.B. McFadden, W.J. Boettinger, Phase-field model for solidification of a eutectic alloy, Proc. R. Soc. Lond. A 452 (1996) 495.
[40] I. Steinbach, F. Pezzolla, B. Nestler, M. Seeßelberg, R. Prieler, G.J. Schmitz, J.L.L. Rezenda, A phase field concept for multiphase systems, Physica D 94 (1996) 135.
[41] J. Tiaden, B. Nestler, H.J. Diepers, I. Steinbach, The multiphase-field model with an integrated concept for modeling solute diffusion, Physica D 115 (1998) 73.
[42] W.T. Kim, S.G. Kim, J.S. Lee, T. Suzuki, Equilibrium at stationary solid–liquid interface during phase-field modeling of alloy solidification, Metall. Mater. Trans. A 32A (2001) 961.
[43] W. Kurz, D.J. Fischer, in: Fundamentals of Solidification, Trans Tech Publications, Aedermansdorf, 1986, p. 178.
[44] J.C. Heinrich, D.W. Pepper, in: Intermediate Finite Element Method: Fluid Flow and Heat Transfer Applications, Taylor & Francis, Philadelphia, 1999, p. 27, 63, 79, 139, 260.
[45] L.A. Hageman, D.M. Young, in: Applied Iterative Methods, Academic Press, New York, 1981, p. 139.
[46] M.J. Vénere, Técnicas adaptivas en cálculo numerico para problemas en dos y tres dimensiones, in: C. Carasso, C. Conca, R. Correa, J.P. Puel (Eds.), Mathématiques Appliquées aux Sciences de l'Ingenieur, CÈDAPUÉS, 1991, p. 411.

[47] E. Dari, G. Buscaglia, Topics on finite element meshes for problems with moving boundaries, in: K. Morgan, E. Oñate, J. Periaux, J. Peraire, O.C. Zienkiewicz (Eds.), Finite Elements in Fluids. New Trends and Applications, Part I, CIMNE, Barcelona, 1993, p. 735.
[48] C. Padra, M.J. Vénere, On adaptivity for diffusion problems using triangular elements, Engrg. Comput. 12 (1995) 75.
[49] M.C. Rivara, M.J. Vénere, Cost analysis of the longest-side refinement algorithm for triangulations, Engrg. Comput. 12 (1996) 224.
[50] M.J. Vénere, R. Saliba, R. Feijóo, Adaptividad tridimensional con mallas no estructuradas, Revista Internacional de Métodos Numéricos para Cálculo y Diseño en Ingeniería 13 (1997) 499.
[51] G.F. Carey, in: Computational Grids; Generation, Adaptation, and Solution Strategies, Taylor & Francis, Washington, DC, 1997, p. 69, 201.
[52] E.A. Dari, M.J. Vénere, A node replacement method for automatic mesh generation, Latin Amer. Appl. Res. 21 (1991) 275.
[53] M.J. Vénere, E.A. Dari, Análisis comparativo de algoritmos para obtener triangulaciones Delaunay, Mec. Comput. 10 (1990) 491.
[54] V. Alexiades, A.D. Solomon, in: Mathematical Modeling of Melting and Freezing Processes, Hemisphere Publishing, Washington, DC, 1993, p. 106.
[55] S.P. O'Dell, G.L. Ding, S.N. Tewari, Cell/dendrite distribution in directionally solidified hypoeutectic Pb–Sb alloys, Metall. Mater. Trans. A 30A (1999) 2159.